INTERNATIONAL JOURNAL FOR NUMERICAL METHODS IN FLUIDS, VOL. 18, 385–413 (1994)

INVESTIGATION OF FLUX FORMULAE IN TRANSONIC SHOCK WAVE/TURBULENT BOUNDARY LAYER INTERACTION

D. DRIKAKIS AND F. DURST

Lehrstuhl für Strömungsmechanik, Universität Erlangen–Nürnberg, Cauerstr. 4, D–91058 Erlangen, Germany

SUMMARY

The aim of the present study is to examine the accuracy and improvement of various numerical methods in the solution of the transonic shock/turbulent boundary layer interaction problem and to show that a significant source of numerical inaccuracies in turbulent flows is not only the inadequacy of the turbulence model but also the numerical discretization. Comparisons between a Riemann solver and a flux-vector-splitting method as well as between various numerical high-order extrapolation schemes with corresponding experimental results are presented.

KEY WORDS Transonic turbulent flows Flux-splitting methods Navier–Stokes algorithms

1. INTRODUCTION

Transonic viscous flow, where the interaction of a shock wave and a boundary layer often leads to extremely detrimental effects, has been studied for several years. Considerable advances have been made in the calculation of the pressure distribution over a body surface where the shock/boundary layer interaction occurs. However, the accuracy of the numerical predictions deteriorates as the interaction strengthens and boundary layer separation occurs. In order to accurately predict the viscous flow behaviour, the correct shock position must be obtained, since the shock position is closely coupled to the viscous flow under separation conditions.[1] The interaction between a shock wave and a boundary layer often amplifies the viscous effects to such an extent that the real flow may differ markedly from the perfect fluid model frequently used to define the shape of the body.[2]

Transonic turbulent separated flows over a bump geometry have been investigated in the past.[1–5] In Reference 1 a comparison of experimental results with numerical solutions obtained using the algebraic Cebeci–Smith model and the two-equation k–ω turbulence model of Wilcox and Rubesin showed that 'the more sophisticated two-equation formulation does not predict substantially different flow behaviour than that predicted with the simple algebraic eddy viscosity model. The numerical solutions delivered poor predictions of the shock location. The same transonic turbulent flow has been studied[3] by other authors using a k–ε model and the Beam–Warming finite difference scheme for the discretization of the fluxes. An improvement in the prediction of the shock location was achieved, but the inaccuracies in the separation region after the shock wave were larger than the corresponding results of Reference 1. Improvements

CCC 0271–2091/94/040385–29

Received December 1992
Revised September 1993

in the above flow simulation have also been achieved by Goldberg and co-workers[4,5] using a new back-flow turbulence model.

A significant reason for the inaccuracies is certainly the turbulence models used in the simulation and it is well known that major improvements are still needed in turbulence modelling before the shock/boundary layer interaction can be reliably treated theoretically.[6] In the present study another aspect is discussed regarding the accuracy and reliability of the prediction of the above physical problem. A question originating from the numerical research is: is the source of the inaccuracies in such complex flows always the turbulence closure models or can the discretization scheme significantly influence the resolution of the physical problem?

During the last two decades, several numerical methods have been developed for the solution of the compressible Euler and Navier–Stokes equations. Among these, flux-vector-splitting (FVS),[7–9] flux-difference-splitting (FDS)[10] and TVD[11] methods have shown very good performance for inviscid flows. In the case of FVS methods, inaccuracies have been observed in viscous flow calculations. The investigation of flux formulae for laminar flows has been carried out in the past for benchmark test cases.[12,13] According to the work of van Leer *et al.*,[12] the first-order Roe FDS scheme is more accurate in the boundary layer than the first-order van Leer FVS scheme. van Leer *et al.*[12] also observed that using MUSCL interpolation, the FVS method showed a clear improvement in the representation of the boundary layer, but comparison with the simple explicit MacCormack scheme showed that the latter remains better than FVS on a medium-fine grid. Modifications and improvements of van Leer splitting have been presented in References 13–15 for laminar viscous flows.

In order to validate and further improve the flux-splitting schemes, a modified Steger–Warming FVS method and a Riemann solver[16] are validated in the present paper for a turbulent flow when a shock/boundary layer interaction occurs. For high-order extrapolation the MUSCL[17] and a five-point extrapolation scheme were employed. Using five-point extrapolation, the accuracy of the FVS method is improved and the method provides similar performance to the Riemann solver. A numerical investigation is also presented on the accuracy of the extrapolation schemes used for the definition of variables on the cell faces. In some cases the extrapolation schemes significantly influence the numerical prediction of the turbulent transonic flow as shown in the present results. The numerical investigation was conducted on the prediction of pressure distribution, velocity and turbulent shear stress profiles in the boundary layer.

2. MATHEMATICAL MODELLING

The complete set of axisymmetric Navier–Stokes equations can be written as follows for a general non-orthogonal curvilinear co-ordinate system using the conservative variables as primitive variables:

$$(JQ)_t + E_\xi + G_\zeta + J\frac{\tilde{G}+\bar{G}}{z} = \frac{1}{Re}\left(R_\xi + S_\zeta + J\frac{\tilde{S}+\bar{S}}{z}\right). \tag{1}$$

The unknown solution vector Q and the flux vectors are written as

$$Q = \begin{pmatrix} \rho \\ \rho u \\ \rho w \\ e \end{pmatrix},$$

$$E = J(\tilde{E}\xi_x + \tilde{G}\xi_z), \qquad G = J(\tilde{E}\zeta_x + \tilde{G}\zeta_z), \qquad R = J(\tilde{R}\xi_x + \tilde{S}\xi_z), \qquad S = J(\tilde{R}\zeta_x + \tilde{S}\zeta_z),$$

with

$$\tilde{E} = \begin{pmatrix} \rho u \\ \rho u^2 + p \\ \rho uw \\ (e+p)u \end{pmatrix}, \qquad \tilde{G} = \begin{pmatrix} \rho w \\ \rho uw \\ \rho w^2 + p \\ (e+p)w \end{pmatrix},$$

$$\tilde{R} = \begin{pmatrix} 0 \\ \tau_{xx} \\ \tau_{xz} \\ u\tau_{xx} + w\tau_{xz} + q_x \end{pmatrix}, \qquad \tilde{S} = \begin{pmatrix} 0 \\ \tau_{zx} \\ \tau_{zz} \\ u\tau_{zx} + w\tau_{zz} + q_z \end{pmatrix},$$

$$\bar{G} = \begin{pmatrix} 0 \\ 0 \\ -p \\ 0 \end{pmatrix}, \qquad \bar{S} = \begin{pmatrix} 0 \\ 0 \\ -\tau_{\theta\theta} \\ 0 \end{pmatrix}.$$

Body-fitted arbitrary co-ordinates (ξ, ζ) are used, while $J = x_\xi z_\zeta - x_\zeta z_\xi$ is the Jacobian of the transformation $\xi = \xi(x, z)$ and $\zeta = \zeta(x, z)$ from Cartesian co-ordinates (x, z) to generalized co-ordinates (ξ, ζ). Using the above transformation, the equations are solved in a computational plane with $\Delta\xi = 1$ and $\Delta\zeta = 1$. The subscripts ξ, ζ, x and z denote partial derivatives, except for the stresses τ_{xx}, τ_{xz}, τ_{zx} and τ_{zz} and the heat terms q_x and q_z. The stresses and heat terms are given as

$$\tau_{xx} = -\frac{2}{3}\mu(-2u_x + w_z) - \frac{2}{3}\mu\frac{w}{z}, \qquad \tau_{zz} = -\frac{2}{3}\mu(u_x - 2w_z) - \frac{2}{3}\mu\frac{w}{z}, \qquad \tau_{xz} = \tau_{zx} = \mu(w_x + u_z),$$

$$\tau_{\theta\theta} = \tfrac{4}{3}\mu(w/z) - \tfrac{2}{3}\mu(\partial u/\partial x + \partial w/\partial z),$$

$$q_x = \left(\frac{\gamma\mu_l}{Pr_l} + \frac{\gamma\mu_t}{Pr_t}\right)T_x, \qquad q_z = \left(\frac{\gamma\mu_l}{Pr_l} + \frac{\gamma\mu_t}{Pr_t}\right)T_z.$$

Here u and w are the Cartesian velocity components in the x- and z-directions respectively, ρ is the density, p is the pressure and e is the total energy per unit volume. The total energy is defined as

$$e = \rho i + 0.5\rho(u^2 + w^2), \tag{2}$$

where i represents the specific internal energy. Re, Pr_l, Pr_t, μ_l, and μ_t are the Reynolds number, the laminar Prandtl number ($Pr_l = 0{\cdot}7$), the turbulent Prandtl number ($Pr_t = 0.9$) and the laminar and turbulent viscosities respectively. The turbulent eddy viscosity is determined from an algebraic turbulence model (see below), while the diminsionless laminar viscosity is defined by the Sutherland law as

$$\mu_l = \frac{110{\cdot}4/T_0 + 1}{110{\cdot}4/T_0 + T}\,T^{3/2}, \tag{3a}$$

where T_0 is the temperature of dimensionalization. The viscosity μ is the sum of the laminar and turbulent viscosities:

$$\mu = \mu_l + \mu_t. \tag{3b}$$

The system of Navier–Stokes equations is completed by an equation of state. In the present study the perfect gas equation of state is used:

$$p = \rho(\gamma - 1)i, \tag{4}$$

where $\gamma = 1{\cdot}4$ is the ratio of the specific heats.

For the solution of the Navier–Stokes equations various finite volume numerical methods have been developed and incorporated into one computational code. For the discretization of the inviscid fluxes the computational code uses either a Riemann solver[16] or a modified Steger–Warming FVS method. A description of the methods is given in Appendix I. A high order of accuracy is obtained using high-order extrapolation schemes for the calculation of the conservative variables on the cell faces. The extrapolation schemes used in the present study are the well-known MUSCL[17] and a five-point scheme. A description of the extrapolation schemes is given in Appendix II. Using high-order extrapolation, the accuracy of the discretization of fluxes is not globally increased. This means that the present Riemann solver and FVS method are second-order-accurate methods using either a third-order or a first-order extrapolation scheme. However, the order of accuracy of the extrapolation is decisive in representing accurately the boundary layer.

In the past inaccuracies in viscous calculations using FVS methods have been observed by several authors.[12,13,15,18,19] MacCormack and Candler[18] have shown that the inaccuracies of the Steger–Warming FVS method are caused by the large numerical mixing of the fluid in the boundary layers, where a fictitious pressure gradient is developed. Koren[19] has also observed that Osher's upwind method gives more accurate results in the boundary layers than does van Leer's FVS. Our experience from inviscid and laminar viscous flows is that the present modified Steger–Warming FVS method and the Riemann solver predict with high reliability the flow behaviour using the third-order five-point scheme.[15,20] Pure second-order extrapolation (without sensor functions) and the MUSCL scheme yield inaccuracies in laminar viscous flows. In the following paragraphs the accuracy of the FVS method and the Riemann solver as well as the improvement of the FVS method are examined for the shock/turbulent boundary layer interaction problem.

The solution of the system of Navier–Stokes equations is obtained by an implicit unfactored method using Gauss–Seidel relaxation.[21] The unfactored implicit solution is followed by a Newton method constructing a sequence of approximations q^ν such that $\lim q^\nu \to Q^{n+1}$, where ν is the subiteration state. A Newton form is obtained by linearization of equation (1) around the known subiteration state ν as follows:

$$\begin{aligned} &J\frac{\Delta q^{\nu+1}}{\Delta t} + (A^\nu \Delta q^{\nu+1})_\xi + (C_{vis}^{th,\nu}\Delta q^{\nu+1})_\zeta = J\frac{Q^n - q^\nu}{\Delta t} - \mathrm{RHS}, \\ &\mathrm{RHS} = E_\xi^n + G_\zeta^n - \frac{1}{Re}(R_\xi^n + S_\zeta^n) + \frac{J}{z}\left(\tilde{G} + \bar{G} - \frac{1}{Re}\tilde{S} - \frac{1}{Re}\bar{S}\right). \end{aligned} \tag{5}$$

The solution at the subiteration level $\nu + 1$ is updated as

$$q^{\nu+1} = q^\nu + \Delta q^{\nu+1}.$$

Four Gauss–Seidel relaxation sweeps are applied on the left-hand side of equation (5) while holding the RHS constant, at the same time one and two Newton subiterations are used for the Euler and Navier–Stokes equations respectively. On the left-hand side of equation (5) the thin layer viscous Jacobian $C_{\mathrm{vis}}^{\mathrm{th},\nu}$ is used for steady state calculations instead of the full viscous

Jacobian, thus saving computational time. The axisymmetric terms of the equations are calculated explicitly. This treatment does not introduce stability problems in the convergence, as has been proven by numerical experiments on various mesh sizes.

3. TURBULENCE MODEL

One of the conclusions in the paper of Johnson *et al.*[1] was that although the two-equation formulation is more sophisticated than the eddy viscosity model, it does not predict substantially different flow behavior. In Reference 3 a comparison between the algebraic Baldwin–Lomax model and the k–ε two-equation model has shown that the former predicts sharp increases and decreases in the turbulent shear stress while the latter predicts gradual changes in the turbulent quantities. However, in the two-equation formulation either the shock position did not agree with the experimental results or the pressure was overpredicted downstream of the shock wave in the separation region. The reason for the differences between the numerical and experimental results was reported as inaccuracies of the turbulence models rather than any deficiencies of the experimental data or the computational mesh.

In the present work we examine the accuracy of an FVS method and a Riemann solver in the resolution of turbulent flows using as a turbulence model the Baldwin–Lomax eddy viscosity model,[22] which is widely used in the aerodynamic community. This model is similar to the Cebeci–Smith model but avoids the necessity of finding the edge of the boundary layer.

4. DESCRIPTION OF THE TRANSONIC TURBULENT FLOW

4.1 Axisymmetric geometry and computational grids

A schematic diagram of the model and its associated flow field is shown in Figure 1(a). The model consists of an annular circular arc bump joined to a thin-walled cylinder of outer diameter 15·2 cm.[1] The bump has a thickness of 1·9 cm and a chord length of 20·3 cm. Its leading edge is joined to the cylinder by a smooth circular arc of radius 18·3 cm which is tangent to the cylinder at 3·33 cm upstream and to the bump at 2·05 cm downstream of the intersection of the arc of the bump and the cylinder.[1] The test conditions of the experiment were a freestream Mach number $M_\infty = 0{\cdot}875$ and a unit Reynolds number $Re/m = 13{\cdot}6 \times 10^6\ \mathrm{m}^{-1}$. With the long initial section of the model and this unit Reynolds number a fully developed turbulent boundary layer was ensured without implementation of a transition strip as reported in Reference 1. A shock wave is formed in the flow field and a separated region is induced by the shock wave. Various sizes of computational grids have been developed in each co-ordinate direction in order to check the influence of the grid on the numerical prediction. The grid sizes used are 82×42, 82×82 and 162×82. Normal to the flow direction an exponentially stretched fine point spacing was used to resolve the part of the flow where viscous effects are important. The distance of the first mesh line from the boundary was selected so that the minimum y^+ is about 0·3. Using such a small distance, the results are independent of this spacing. When 42 and 82 grid points are used in the normal direction, 35 and 62 points are contained in the viscous layer respectively. The boundaries of the computational mesh are extended 80·3 cm upstream of the bump leading edge and 101·5 cm downstream of the bump trailing edge. For the outer boundary numerical experiments have been conducted to ensure that the outer distance does not influence the flow field. It has been found that the shock wave and separation region remained unchanged when the distance of the outer boundary was greater than 2·5 chords from the solid wall. The present

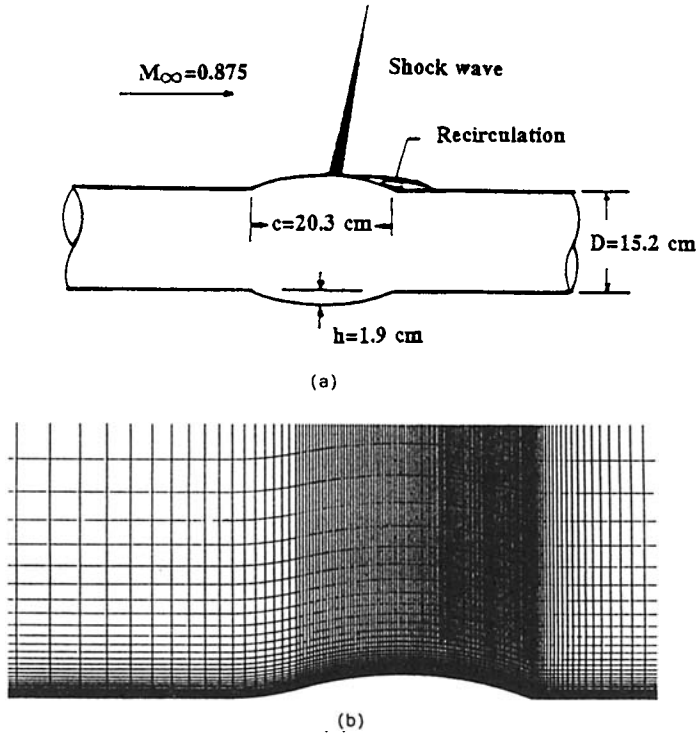

Figure 1. Shock wave/turbulent boundary layer interaction problem: (a) model geometry; (b) enlargement of the 162 × 82 grid over the geometry

solutions are for an outer boundary located at 3 chords from the solid wall. An enlargement of the finest computational mesh (162 × 82) over the bump is shown in Figure 1(b).

4.2 Boundary conditions

At the upstream boundary, freestream boundary conditions are specified. The downstream boundary is positioned far enough away from the interaction region that all gradients in the flow direction can be set equal to zero. No-slip boundary conditions are prescribed on the solid wall and a constant temperature wall is considered. At the outer boundary, calculations using freestream boundary conditions and inviscid solid wall boundary conditions have been compared. The numerical experiments showed that the flow remained unchanged using either the first or second type of the above boundary conditions. The upwind extrapolation scheme uses five computational volumes for the definition of the conservative variables at the cell faces. Fictitious volumes into the solid wall are used in order to define the conservative variables at the solid boundary. These volumes are calculated by extrapolation of the values from the inner flow field.

5. NUMERICAL PREDICTIONS OF THE HIGHER-ORDER METHODS

In the following subsections, comparisons between various computational methods and experimental results[1] are presented. Numerical predictions are presented for the pressure, velocity

and turbulent shear stress profiles and the skin friction distribution. A physical picture of the flow field is shown in Figures 2(a) and 2(b), where the iso-Mach lines and the velocity vectors have been plotted. From these figures the formation of the shock wave and the interaction with the boundary layer can be observed. In addition, the velocity vectors show the deceleration of the flow in the region of the shock and the formation of the separation region. Reattachment occurs downstream of the trailing edge of the bump. It is noted that the velocity vectors have been plotted every eight volumes of the computational mesh in order to be observable in the separation region.

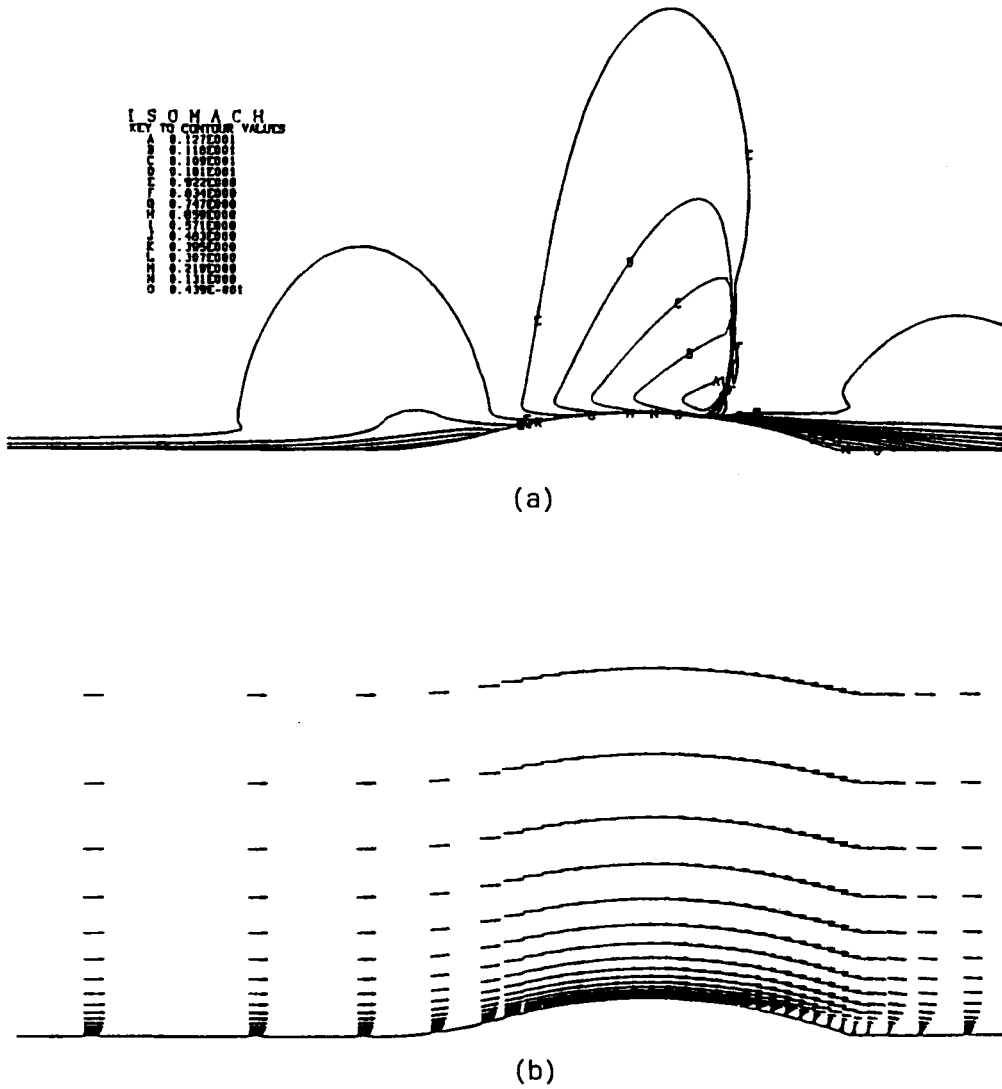

Figure 2. (a) Iso-Mach lines and (b) velocity vectors over the bump

5.1. *Pressure distribution*

The prediction of the correct pressure distribution on the surface of a body under transonic flow conditions is of crucial importance for the determination of the lift and moment. Visualization from experimental results and examination of wall pressure distributions[2] have shown that the interaction domain can be divided into two regions. The first region is the most upstream part of the interaction where a continuous and rapid compression of supersonic nature occurs. The second region is downstream of the shock wave and is of subsonic nature. The flow structure results from the effect far downstream and the shape and curvature of the wall. Considering the above, it is concluded that the behaviour of the shock-boundary layer interaction phenomenon is dependent on the first region of supersonic nature.

The calculation of the pressure distribution and the determination of the correct shock position are connected with the maximum Mach number before the shock wave.[2] In Figures 3(a)–3(d) comparisons between the present numerical predictions and experimental results[1] are presented. In detail, Figures 3(a) and 3(b) show comparisons for various grid sizes using the Riemann solver and the third-order hybrid scheme. The pressure distribution seems to remain almost unchanged with increasing grid size. The results show that the pressure is captured very well downstream of the shock wave in the separated region. Small discrepancies are seen in the capturing of the shock position as well as a slightly lower pressure value before the shock wave. The same behaviour exists when the FVS method with the third-order upwind or the FVS method with the MUSCL scheme is used in the calculations (Figure 3(c)). On the other hand, comparisons (Figures 3(a) and 3(b)) of the present results with the corresponding pressure predictions of References 1 and 3 show that the present predictions are in general closer to the experimental results.

The differences between the present numerical procedures and the procedures of References 1 and 3 are the numerical methods for discretization of the equations as well as the turbulence models. The present algebraic model is theoretically less sophisticated than the k–ω and k–ε models of References 1 and 3. From these results it is clear that the only reason for the better present pressure prediction is the numerical method. In addition, the order of accuracy of the upwind extrapolation seems to influence the pressure prediction (Figure 3(d)). First-order accuracy causes inaccuracies in the determination of the shock positions as well as overprediction of the pressure in the separated region, while second- and third-order schemes present similar behaviour. It is important to note that in Reference 3 the calculations have also been conducted using the Baldwin–Lomax turbulence model, but the present results using the same model are in better agreement with the experimental results. Comparisons of these calculations with the present results are shown in Figure 3(a)).

The situation of shock-induced separation occurs when the maximum Mach number in front of the shock is about 1·3. The slightly lower pressure value in the present results compared with the experiment can be explained by the presence of a higher Mach number than the experimental one ($M = 1{\cdot}32$) in the supersonic region. The present predictions calculate the Mach number just upstream of the shock to be $M = 1{\cdot}3224$. This prediction is very close to the experimental value ($M = 1{\cdot}32$). The numerical prediction of Reference 1 using the k–ω and Cebeci–Smith model was approximately $M = 1{\cdot}4$.

5.2 *Numerical predictions of velocity profiles*

Several comparisons between numerical predictions and experimental results have been obtained for the velocity profiles. Initially, calculations were carried out using the Riemann solver in combination with first-, second- and third-order-accurate extrapolation schemes.

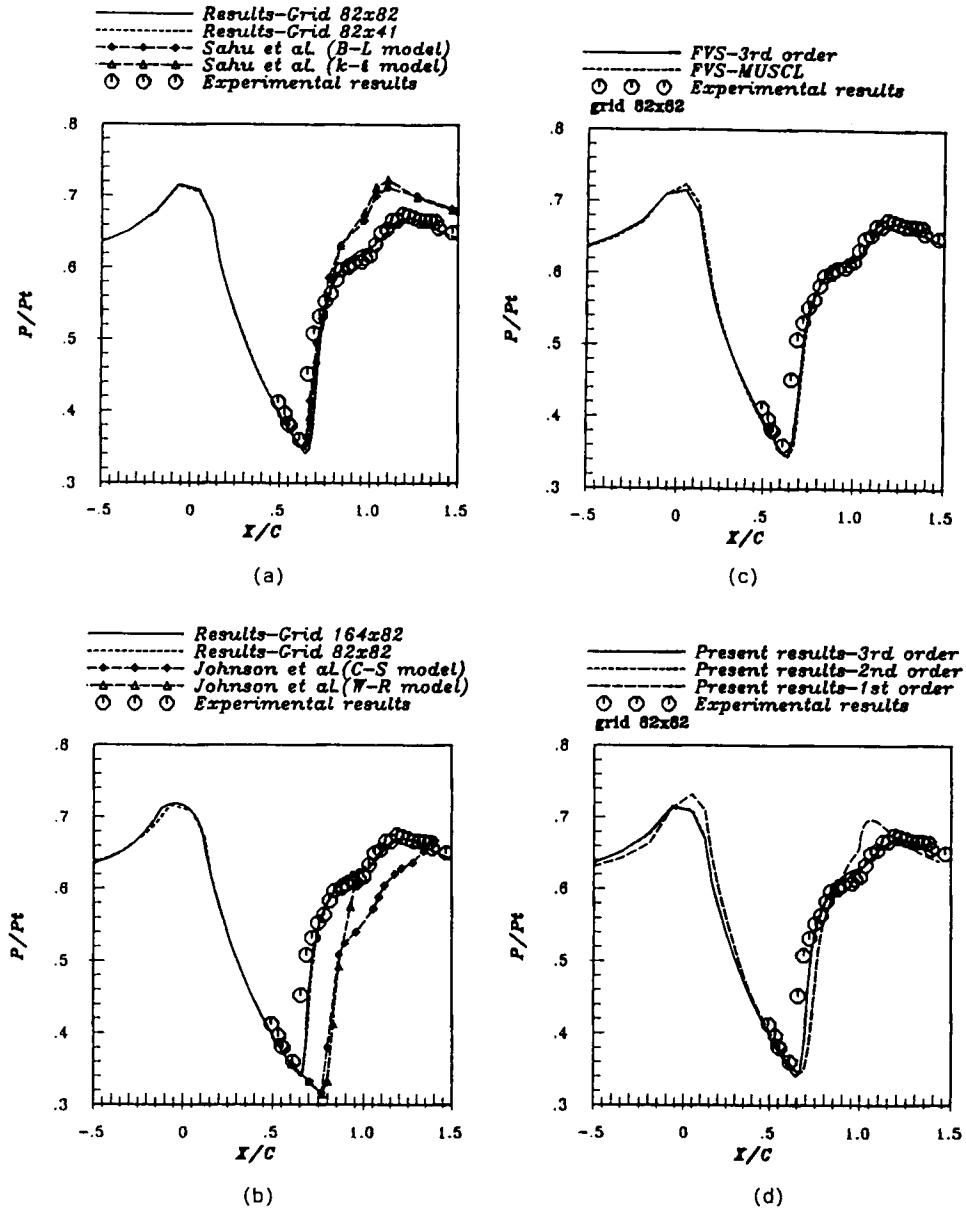

Figure 3. Surface pressure distributions: (a) present results on 82 × 82 and 82 × 42 grids and numerical predictions of Sahu and Danberg;[3] (b) present results on 162 × 82 and 82 × 82 grids and numerical predictions of Johnson *et al.*;[1] (c) present predictions using the FVS method; (d) present predictions using first-, second- and third-order-accurate Riemann solver (B–L: Baldwin–Lomax model; C–S: Cebeci–Smith model; W–R: Wilcox–Rubesin (k–ω) model)

Comparisons of the numerical predictions with the corresponding experimental results are presented in Figures 4 and 5, while in Figures 6 and 7 comparisons between various grid sizes using the third-order 'version' of the Riemann solver are presented. In Figures 4, 5, 6 and 7 U_0 is the freestream velocity. The velocity profiles are compared for various grid stations in the separation region and after the reattachment. For the experimental positions $x/c = 1{\cdot}25$ and

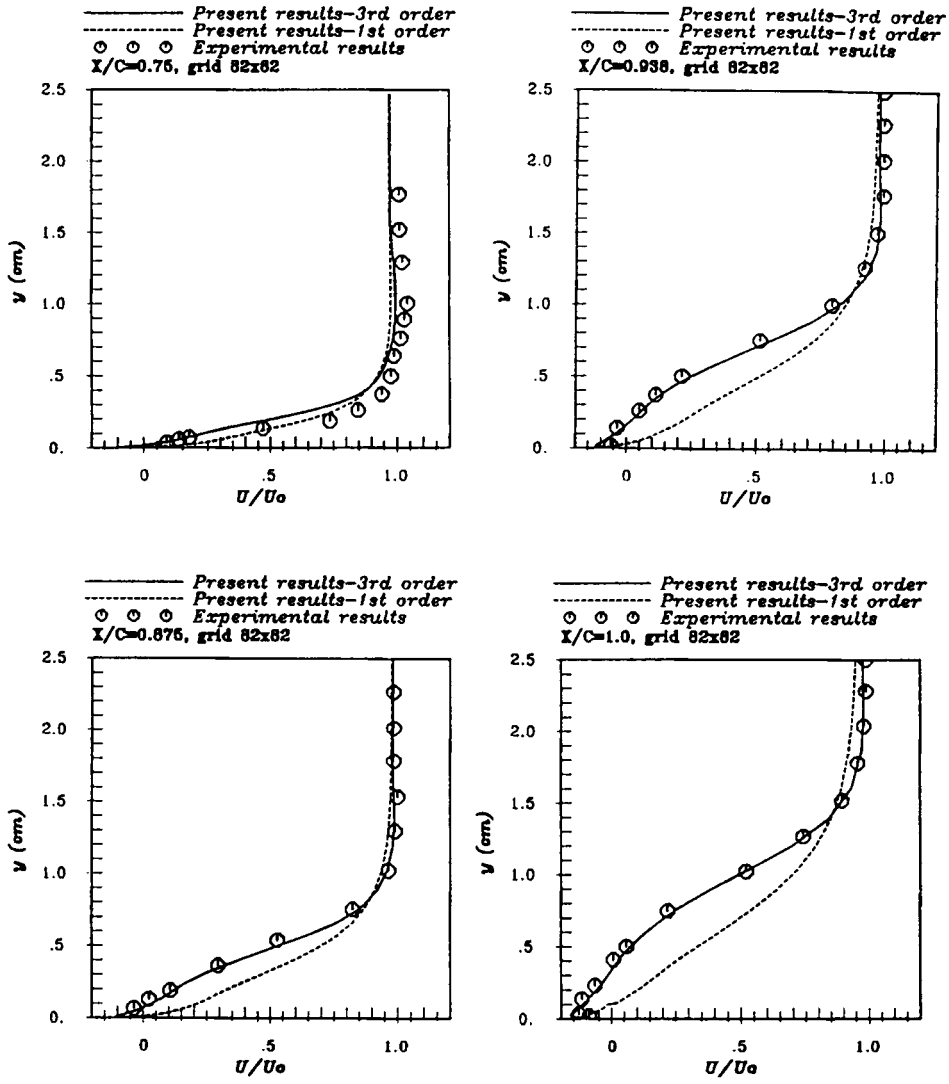

Figure 4. Comparisons of velocity profiles between numerical predictions using the third- and first-order Riemann solver and experimental results

1·375 the profiles have been plotted for two different grid stations in order to avoid interpolation between the present grid positions. At the other stations the grid position coincided within 1% with the corresponding experimental one. For the sake of clarity the profiles for the second-order extrapolation scheme (Figure 5) are plotted separately from the corresponding ones of the third- and first-order schemes. In accordance with the above plots, using the third-order 'version' of the Riemann solver, the numerical predictions for the velocity profiles are in satisfactory agreement with the experiments. It is evident that the first-order scheme leads to misprediction of the velocity profile. The inaccuracies introduced by the first-order scheme are significantly

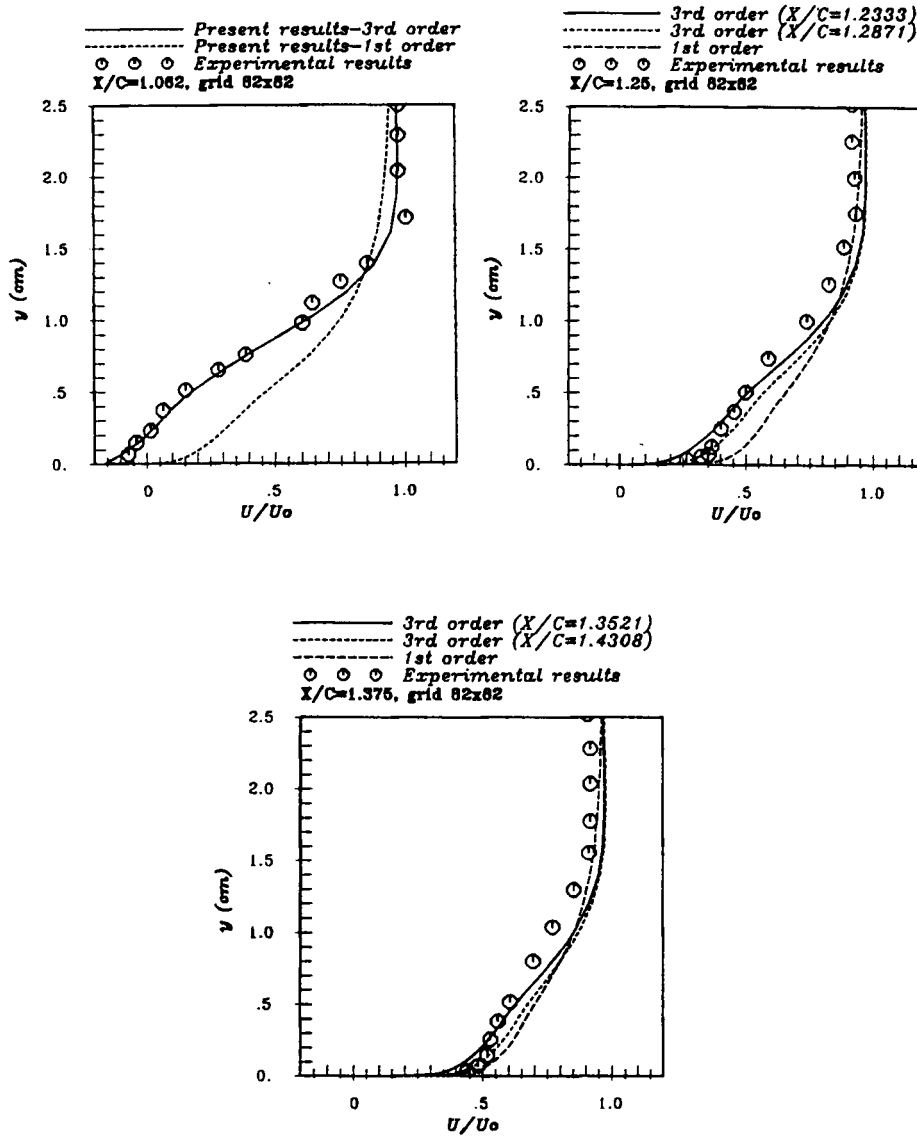

Figure 4. (*continued*)

greater in the separation region (see stations $x/c = 0.875$, 0.938, 1.0 and 1.062). The first-order scheme does not predict the change in the curve of the velocity profile and predicts only negative velocity values in the separation region with a smooth transition up to the positive values of the outer freestream. On the other hand, using the second-order extrapolation, the results do not differ from the corresponding ones using the third-order scheme, predicting the turbulent boundary layer with satisfactory accuracy.

The above comparisons are for the 82 × 82 grid. Comparisons with the finer (162 × 82) and coarser (82 × 42) grids in Figures 6 and 7 show the dependence of the profiles on the grid size. In detail, the results on the finer grid do not show significant differences from the 82 × 82 grid.

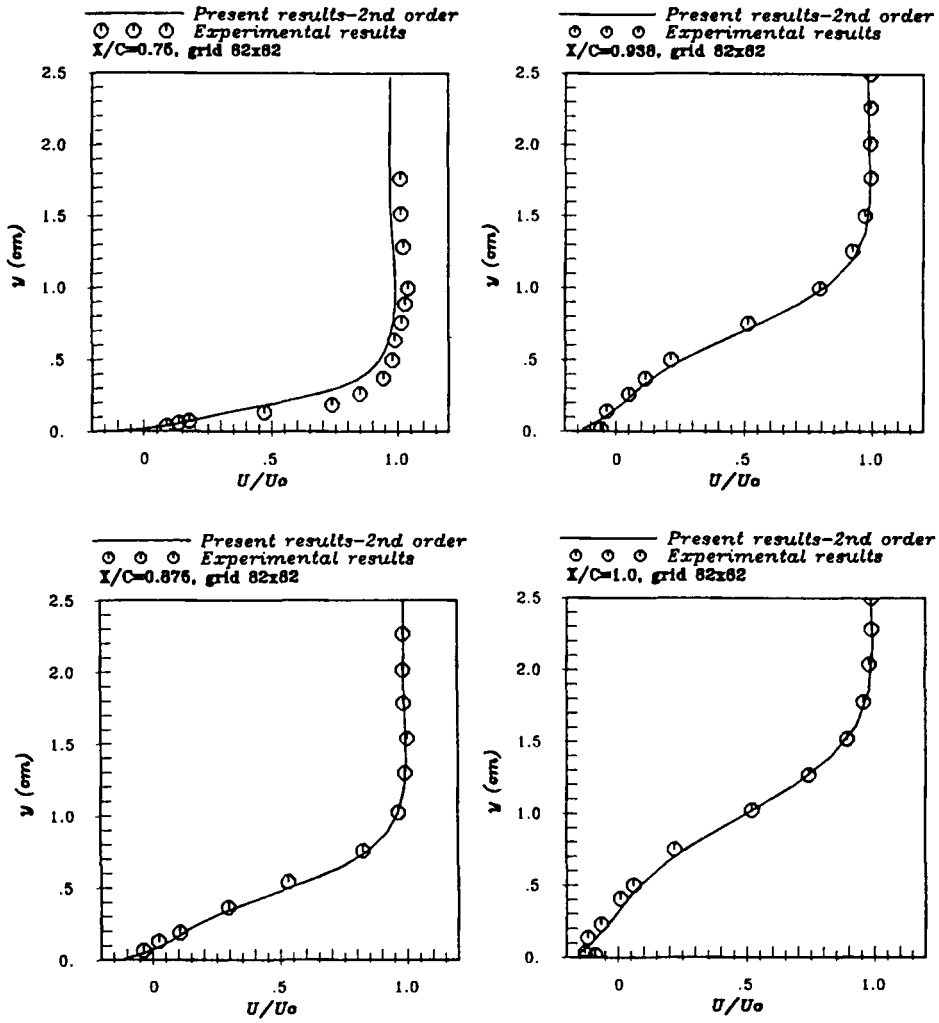

Figure 5. Comparisons of velocity profiles between numerical predictions using second-order Riemann solver and experimental results

All the observable small differences occur in regions of the curve of the profiles. Similar differences in the curve of the profiles are also evident by comparing the results between the 82 × 42 and 82 × 82 grids (Figure 7). In conclusion, we can say that both the 162 × 82 and 82 × 82 grids capture the velocity distribution satisfactorily in the turbulent boundary layer.

The same calculations have also been conducted for the FVS method in combination with the third-order scheme as well as with the MUSCL scheme. In order to limit the size of the paper, results are presented only for the FVS–third-order and FVS–MUSCL methods on the 82 × 82 grid (Figure 8). It is important for the reader to note that numerical experiments have also been carried out using different versions of the MUSCL scheme (fully upwinded, symmetric, third-order-biased and centred). Differences were not observed using the various versions of the scheme. Comparisons between the third-order and MUSCL schemes show that the former predicts the velocity distributions in closer agreement with experiment. This is true

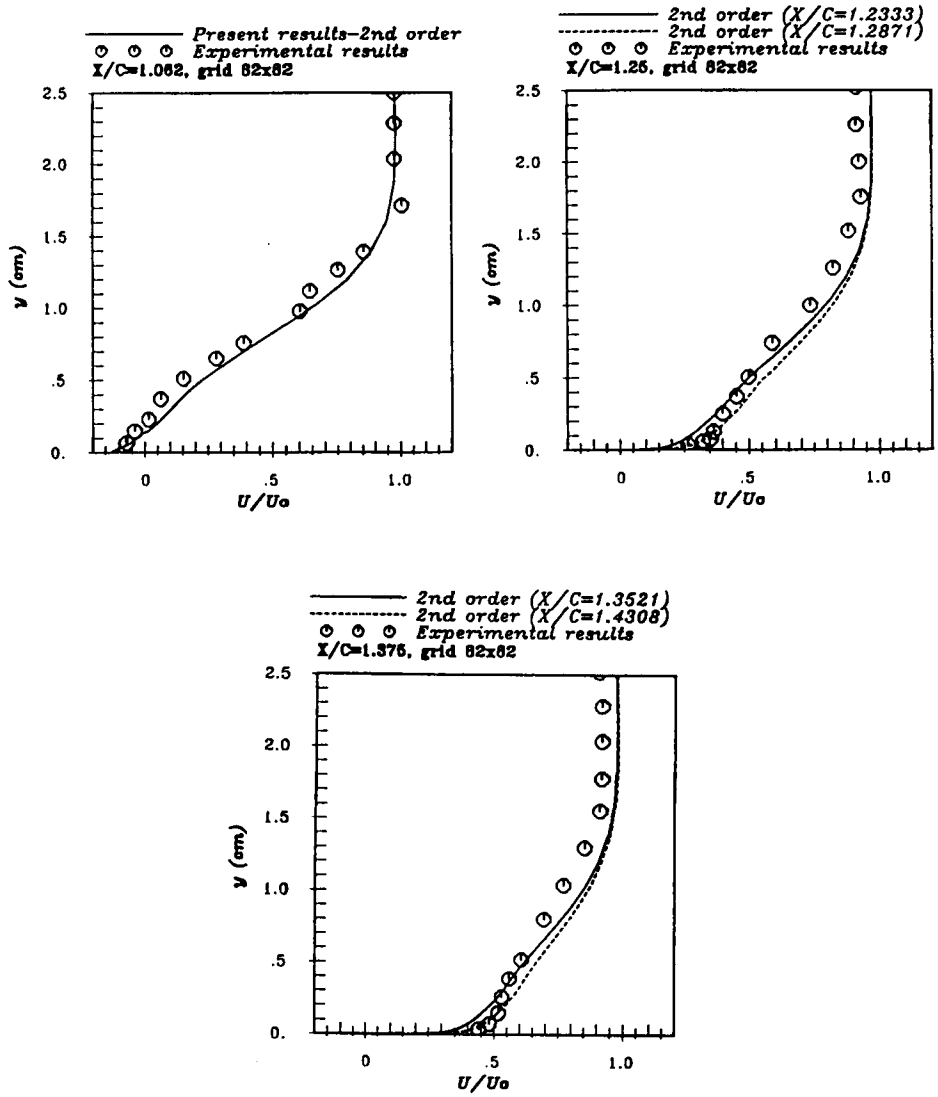

Figure 5. (*continued*)

for all stations of the comparisons except for the station $x/c = 0.75$ just downstream of the shock wave and after the beginning of separation. In this position the MUSCL scheme predicts higher velocities in the region of high curvature of the velocity profile. Comparisons of the profiles in Figures 4 and 8 show that the FVS–third-order method and the Riemann solver with third-order extrapolation yield similar behaviour in the prediction of velocity distributions in the turbulent boundary layer.

The present results have also been compared with the numerical predictions of References 1 and 3. In order to limit the size of the paper, we do not present additional figures with a direct comparison. On the other hand, observations on the present results and those of References 1 and 3 can be made. From these observations it can be concluded that although the eddy viscosity

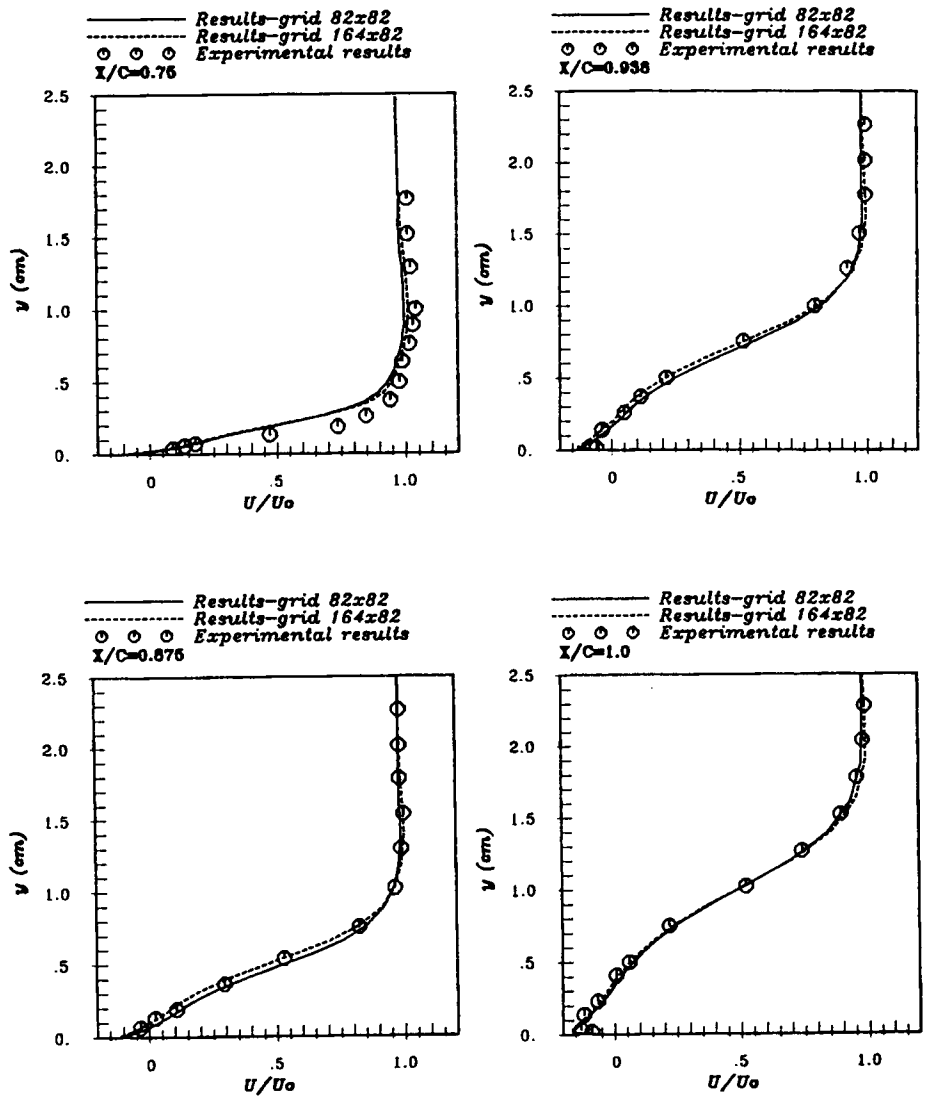

Figure 6. Comparisons of velocity profiles between numerical predictions using 162 × 82 and 82 × 82 grids and experimental results

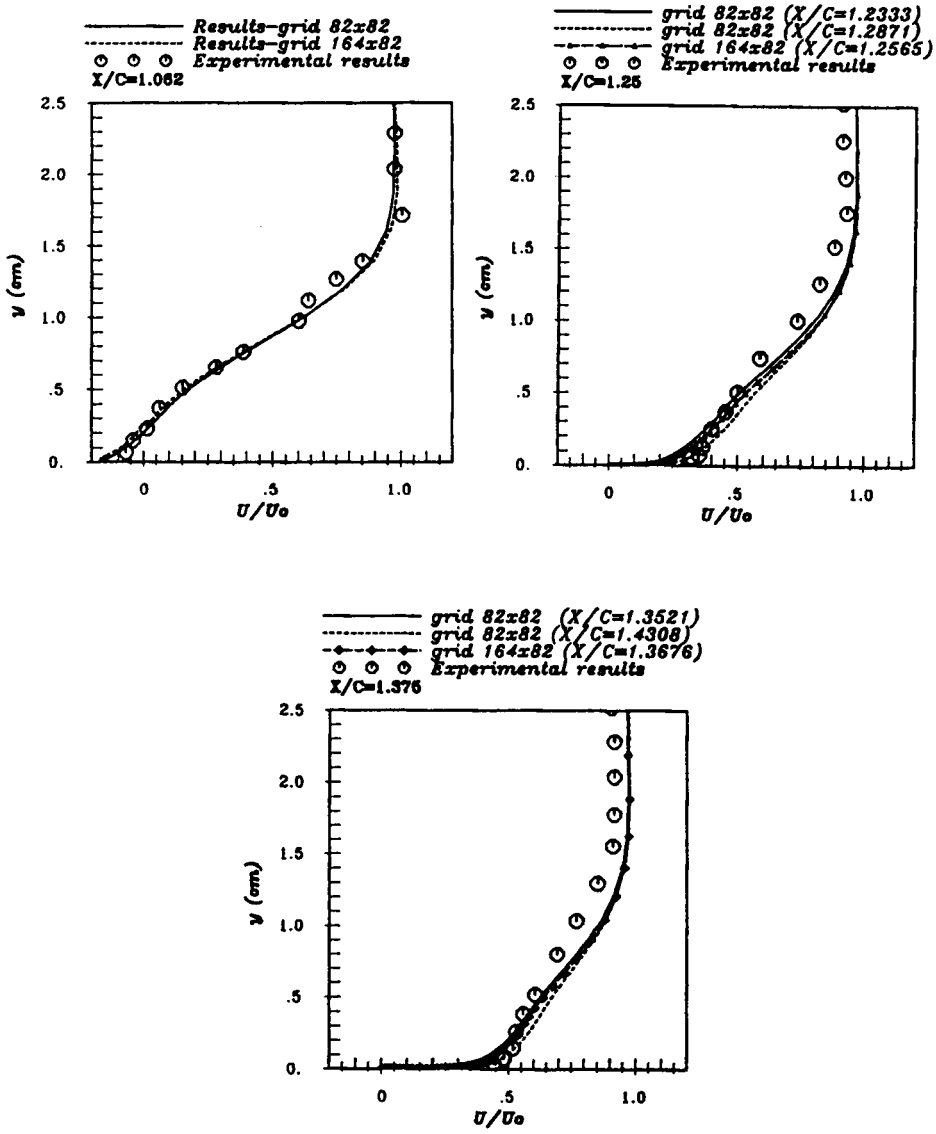

Figure 6. (*continued*)

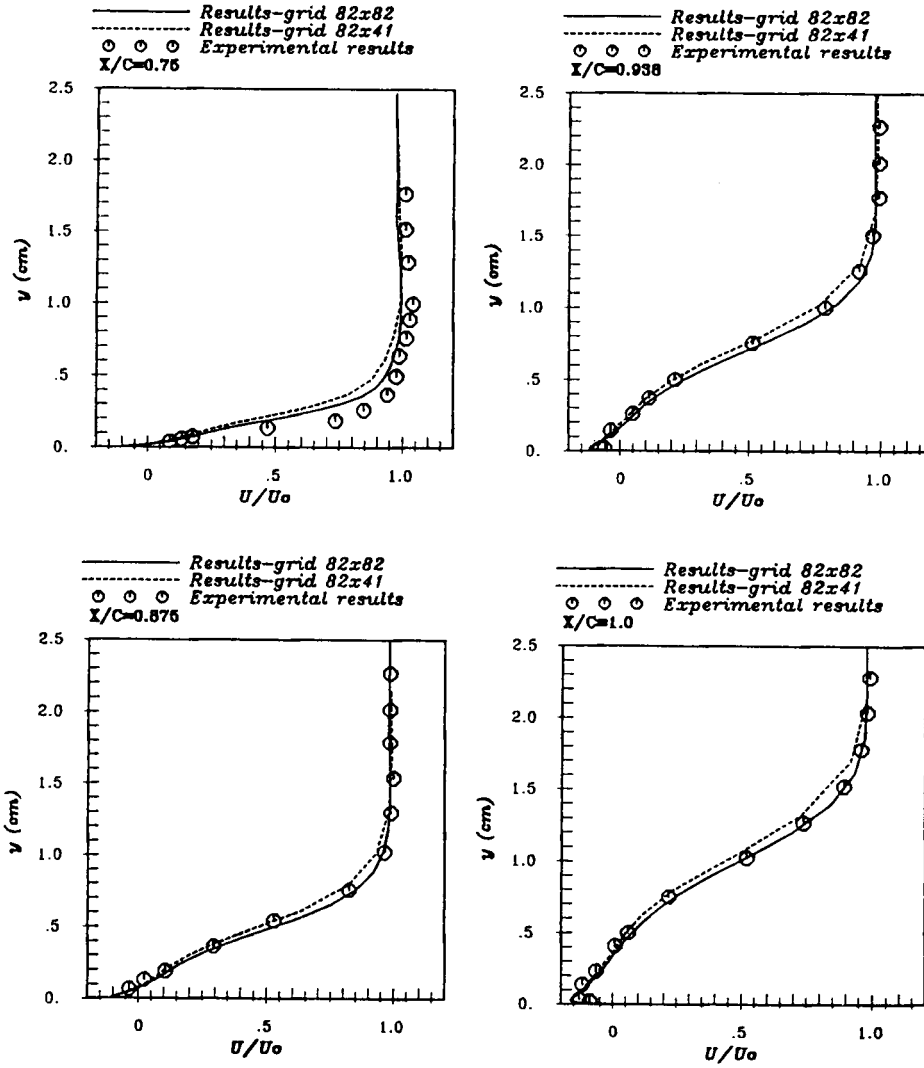

Figure 7. Comparisons of velocity profiles between numerical predictions using 82 × 82 and 82 × 42 grids and experimental results

model was used in the present work, the results for the velocity profiles are generally in better agreement with the experiment than the corresponding ones of References 1 and 3. In detail (see also References 1 and 3), the Baldwin–Lomax turbulence model of Reference 3 predicts significantly worse results than those of the present calculations. In addition, although the k–ε model of Reference 3 improves the velocity predictions, the results have larger differences than the present corresponding results. Our conclusion is that the closer agreement of the present results with the experiment is due to the 'high-order' upwind methods when the less sophisticated eddy viscosity model is used. The basic conclusions on the numerical methods used in the above calculations will be summarized at the end of the paper.

5.3 Numerical predictions of the turbulent shear stress

In the previous subsections the accuracy of the higher-order methods with regard to the pressure distribution, velocity profiles and prediction of the shock values (pressure rise, Mach number just upstream of the shock) has been examined. Before the development of more sophisticated turbulence models, a comprehensive evaluation of the accuracy of the numerical methods for all flow quantities is necessary. The literature on compressible flows contains a limited number of comprehensive studies on the numerical accuracy of methods that have been developed or extended in the last decade to turbulent compressible flows. On the other hand, there are several articles that elaborate the accuracy and improvement of methods for shock waves. In the field of transonic turbulent flows, comparisons between various computational codes have been presented in a viscous transonic aerofoil workshop.[24] One of the conclusions of the above workshop was that more complete experiments for validation of CFD codes are needed in order to help the development of turbulence models and to more completely validate the physical and numerical model errors associated with CFD computer codes.

In order to further evaluate the reliability of the Riemann solver, FVS method and extrapolation schemes, comparisons between numerical predictions and experimental results for the turbulent shear stress are shown. It is necessary to note that the significance of the turbulence modelling for the resolution of such quantities cannot be ignored. Our intention is only to evaluate the order of the inaccuracies introduced by the higher-order methods in the calculation of turbulent flow quantities. The numerical predictions for the turbulent shear stress and comparison between the present methods are shown in Figure 9. The results are for the 162×82 grid. During the development of the present study, numerical experiments on the 82×82 grid were carried out, but only small differences from the 162×82 grid results were observed.

The first observation from Figure 9 is that although the predictions are relatively close to the experiments in the positions just before and after the separation (stations $x/c = 0{\cdot}688$, $0{\cdot}75$ and $0{\cdot}813$), differences exist in the remaining positions. In these regions the methods cannot capture large rises of the shear stress into the turbulent layer. Another observation is that the numerical methods used predict a different rise of the turbulent shear stress. The FVS method with third-order extrapolation seems to predict higher shear stresses than the MUSCL scheme. The Riemann solver with third-order extrapolation yields results closer to the FVS–third-order scheme. The location of the peak shifts further away from the wall and is captured better when the FVS method with third-order extrapolation is used. In Figure 10 comparisons of the results using the different-order extrapolation schemes are shown. The third- and second-order-accurate schemes present small differences. On the other hand, larger inaccuracies are shown using the first-order extrapolation scheme.

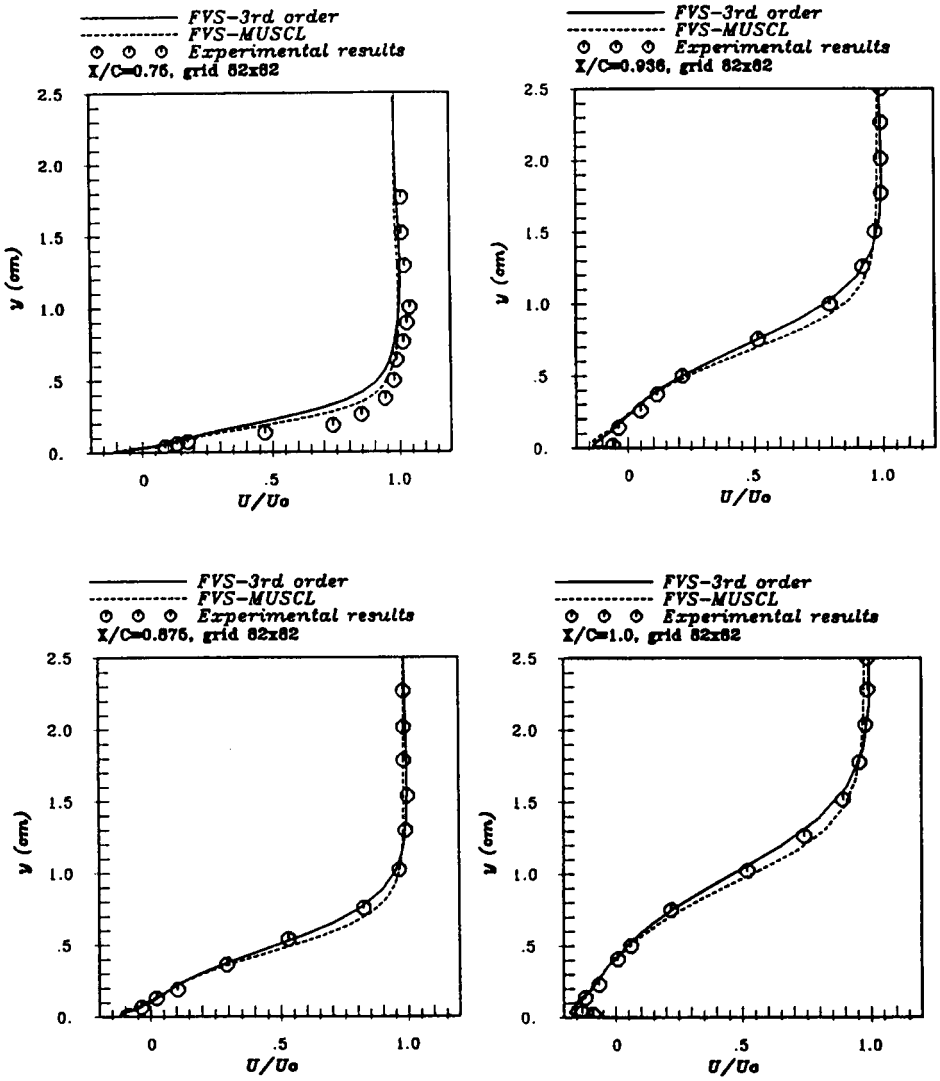

Figure 8. Comparisons of velocity profiles between numerical predictions using FVS–third-order and FVS–MUSCL schemes and experimental results

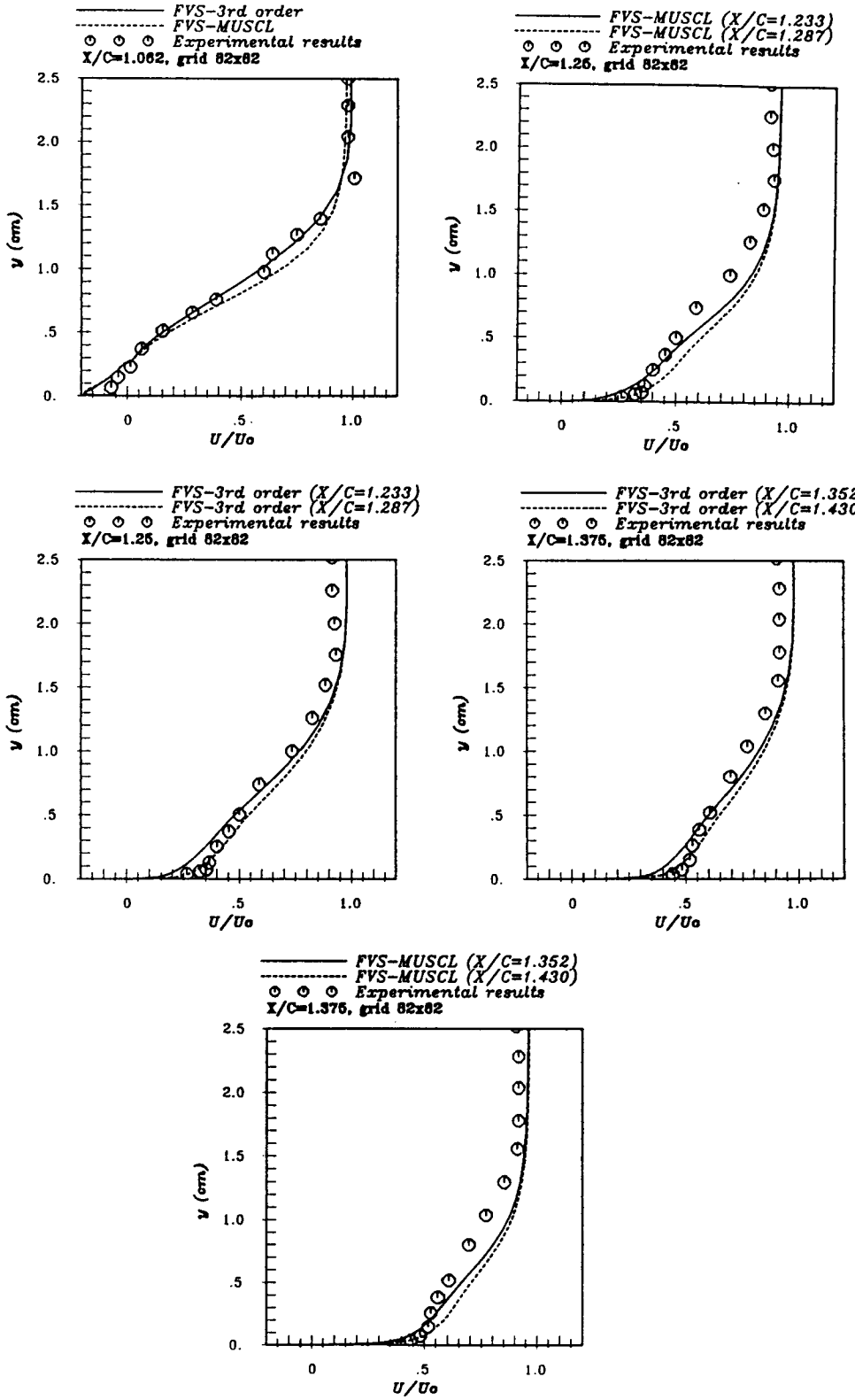

Figure 8. (*continued*)

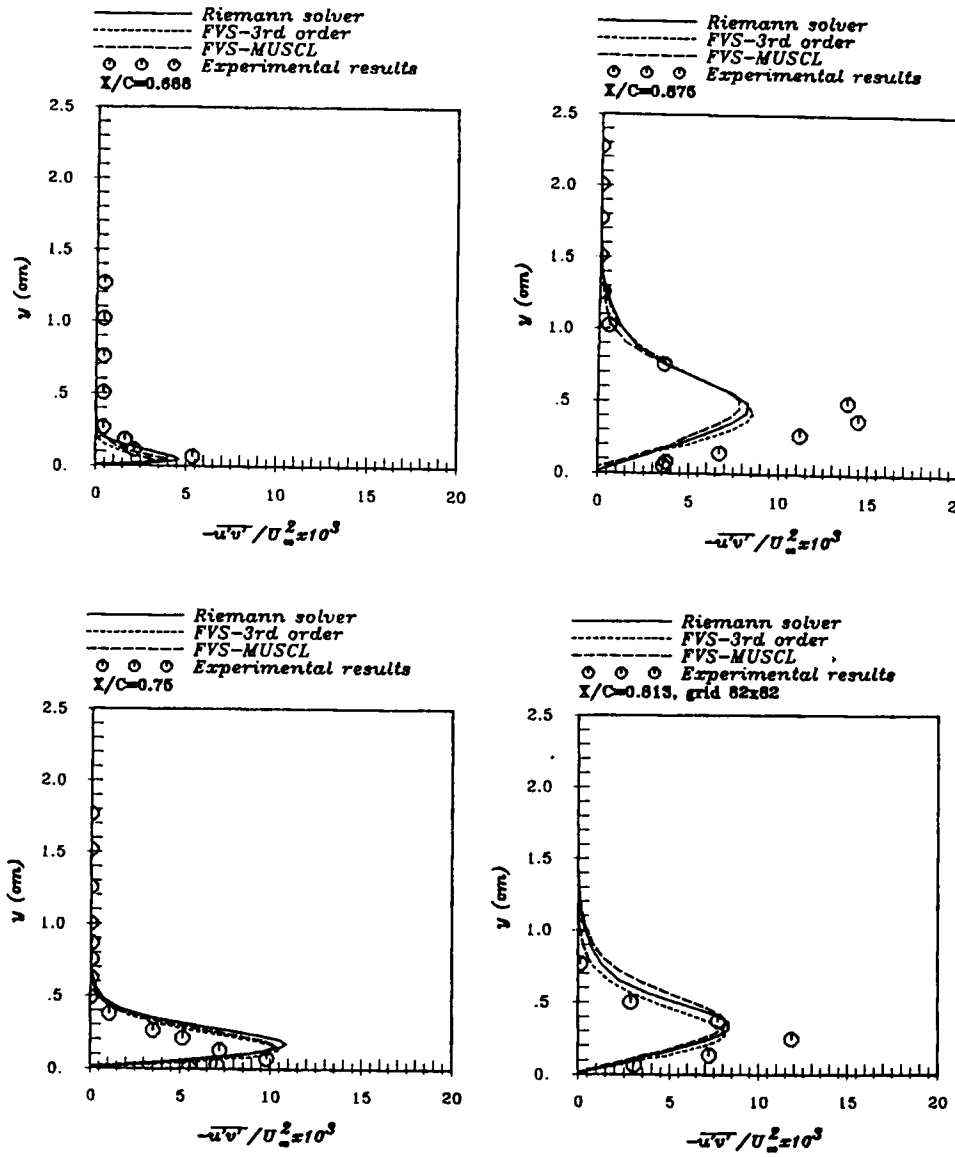

Figure 9. Comparisons of turbulent shear stress profiles between numerical predictions and experimental results

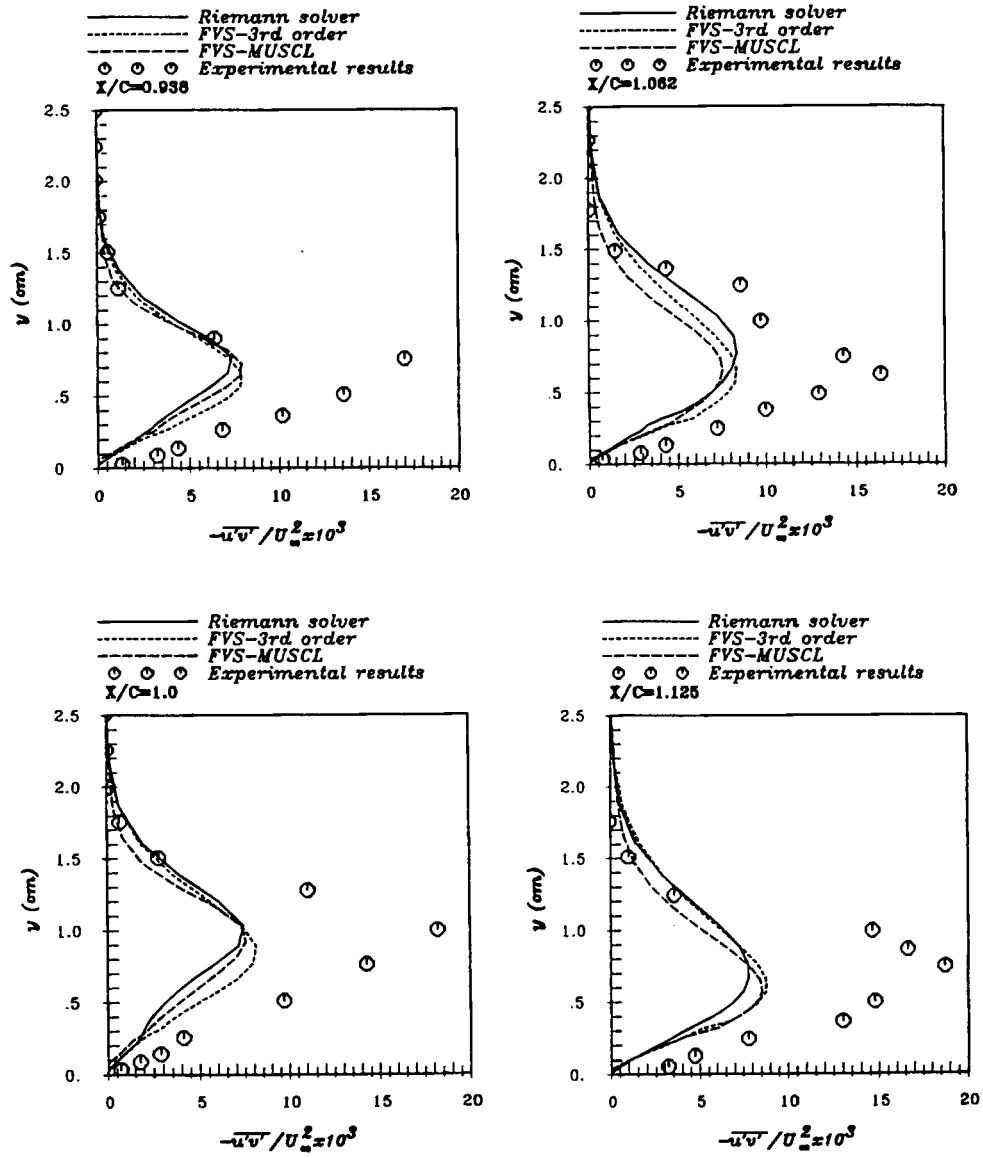

Figure 9. (*continued*)

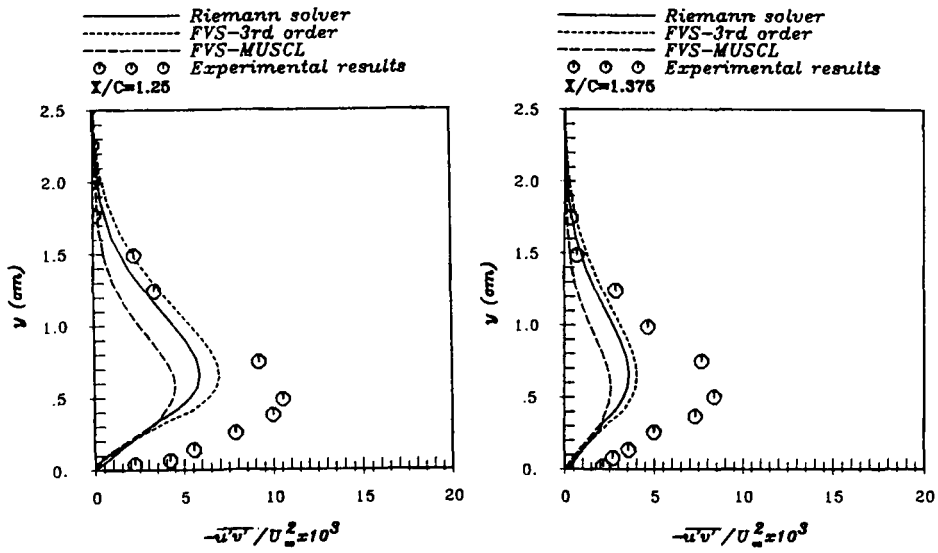

Figure 9. (*continued*)

Table I. Comparisons between present predictions and experimental data for separation and reattachment positions

	Separation position	Reattachment position
Experiment	$x/c \approx 0{\cdot}7$	$x/c \approx 1{\cdot}10$
Riemann solver–third-order	$x/c = 0{\cdot}689877$	$x/c = 1{\cdot}152$
Riemann solver–second-order	$x/c = 0{\cdot}689876$	$x/c = 1{\cdot}152$
Riemann solver–first-order	$x/c = 0{\cdot}731205$	$x/c = 1{\cdot}044$
FVS method–third-order	$x/c = 0{\cdot}689876$	$x/c = 1{\cdot}188$
FVS method–MUSCL	$x/c = 0{\cdot}689876$	$x/c = 1{\cdot}152$

The differences between the calculations and the experiments for the turbulent shear stress prediction can only be explained by the inaccuracies introduced by the turbulence model. The present shear stress predictions are in close agreement with those of Reference 3 where the k–ε model was used. In addition, the present results are in better qualitative agreement with the experiments than those of Reference 3 obtained using the Baldwin–Lomax model. The explanation of the latter is the higher accuracy offered by the present numerical methods.

In Figure 11 the skin friction distribution for various grid sizes is shown. The results are Riemann solver predictions. The experimental results predict separation at the position $x/c \approx 0{\cdot}7$ and reattachment at the position $x/c \approx = 1{\cdot}10$. The present numerical predictions are given in Table I. The results show satisfactory agreement with the experimental values.

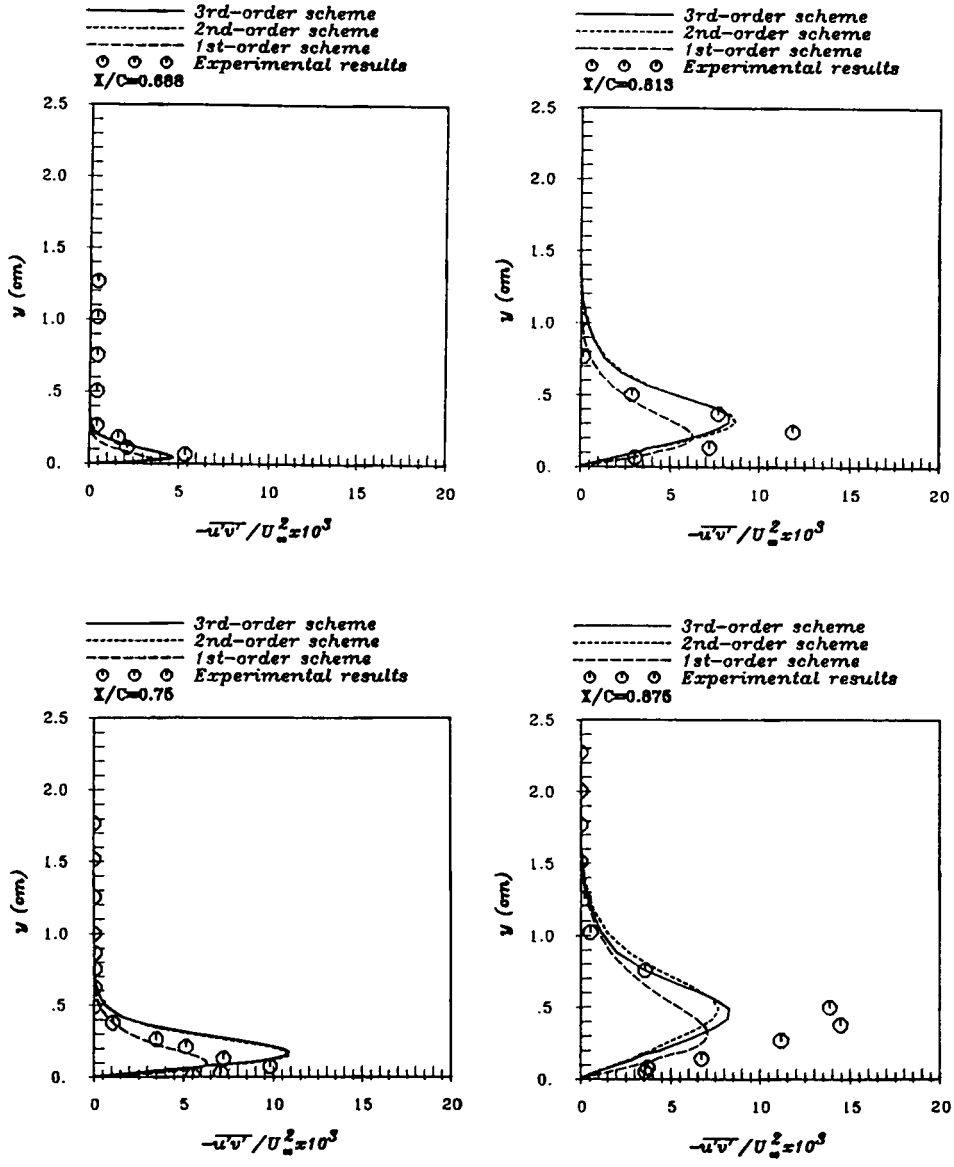

Figure 10. Comparisons of turbulent shear stress profiles between numerical predictions using different-order accuracies of Riemann solver and experimental results

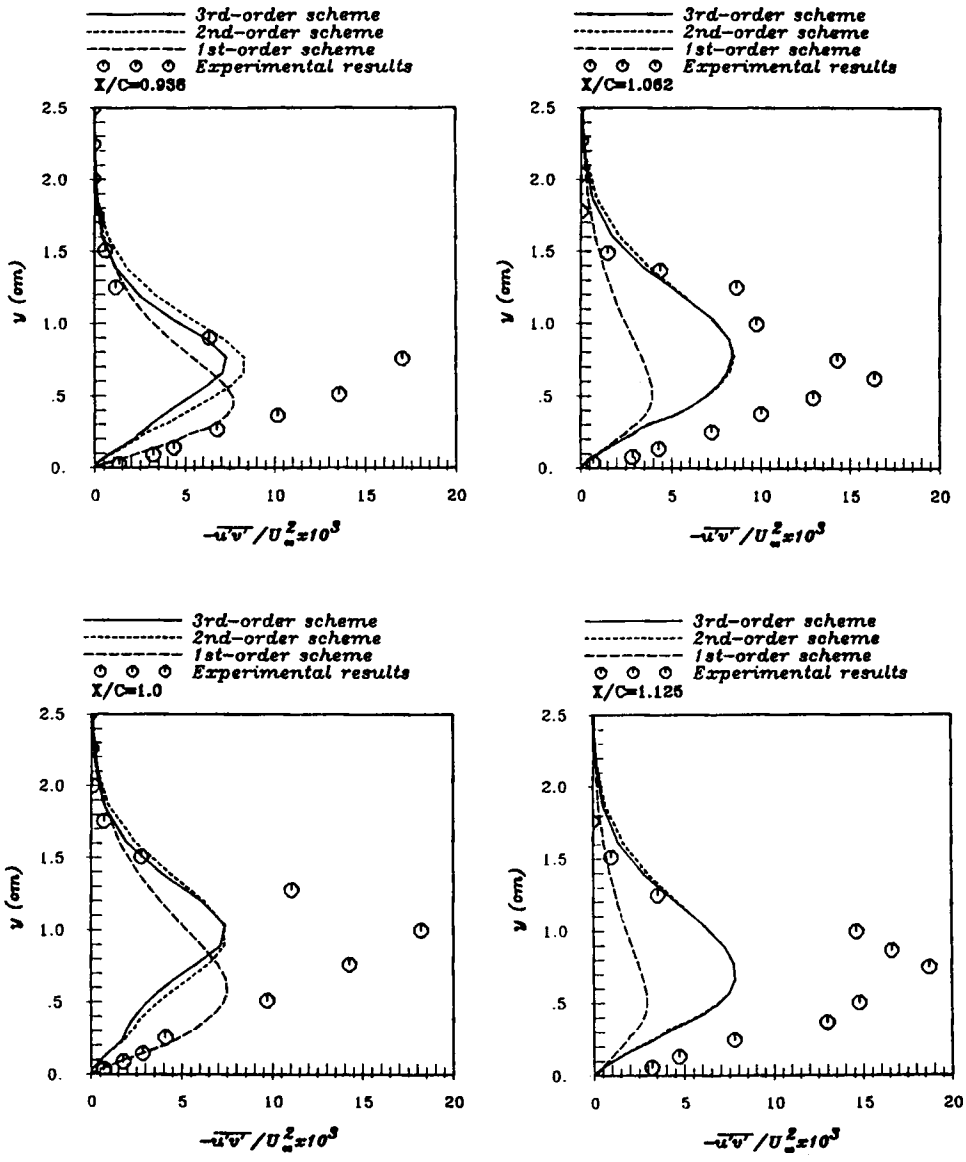

Figure 10. (*continued*)

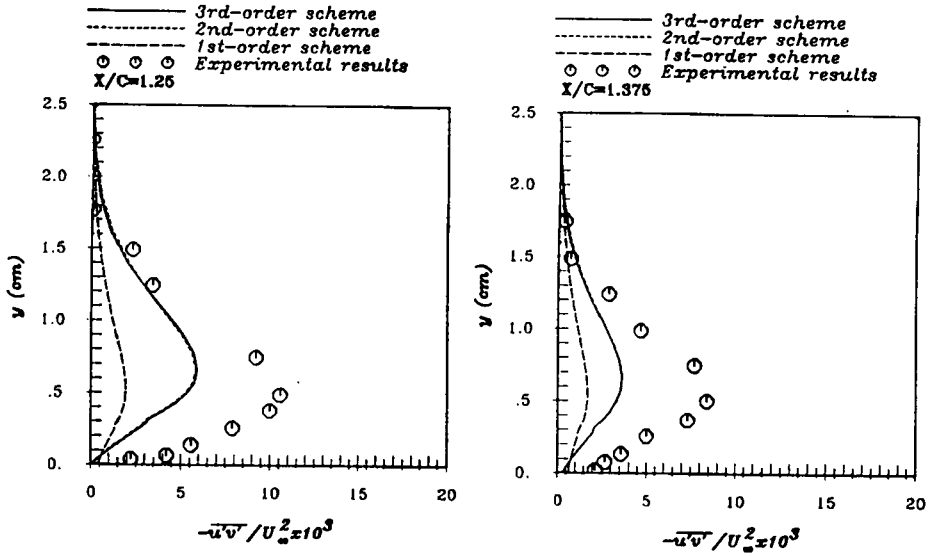

Figure 10. (*continued*)

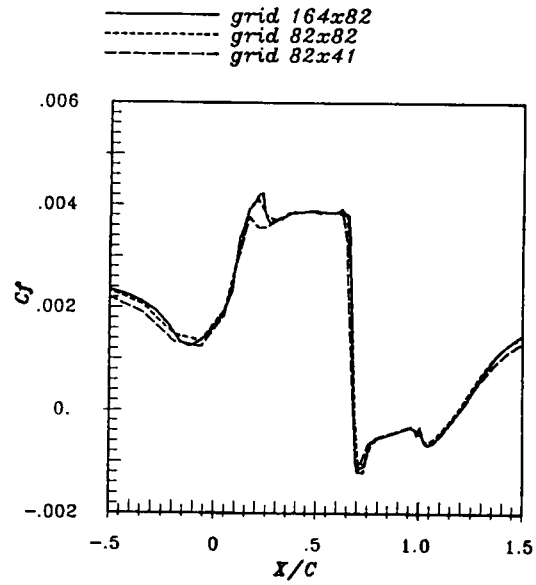

Figure 11. Skin friction distribution

6. CONCLUSIONS

In the present work the accuracy of flux formulae in the prediction of shock/turbulent boundary layer interaction was examined. The basic conclusions from the present study are as follows.

1. The five-point scheme gives closer agreement with the experimental results than the MUSCL scheme. Five-point extrapolation improves the performance of the FVS method.
2. The third-order five-point scheme does not show significant differences from the second-order scheme. Large inaccuracies are introduced by the first-order scheme.
3. The FVS method and the Riemann solver show similar behaviour in the prediction of the turbulent flow.
4. The present predictions for the pressure and velocity distribution are in close agreement with the experimental results even though an algebraic turbulence model is used. The shock wave is captured close to the experimental measurements. The velocity profile predictions generally show better agreement with the experiments than the corresponding predictions in the literature.
5. The present predictions for the turbulent shear stress show similar behaviour to the corresponding prediction in the literature. The present results are in close agreement with the numerical results of Reference 3 when the k–ε model is used. In addition, using the Baldwin–Lomax model, the present results show closer agreement with the experimental results for the turbulent shear stress than the results of Reference 3 where the same model is used.

The investigation of new numerical methods for compressible flows (based on the Boltzmann approach) as well as turbulence models other than the present one is intended to be validated in turbulent transonic flows in order to improve the numerical resolution of such complex flows.

ACKNOWLEDGEMENTS

The financial support from the Bavarian Ministry of Education and the Bavarian Science Foundation is greatly appreciated. The computing time on the Meiko and Parsytec transputer systems was provided by the Bavarian Centre of High Performance Scientific Computing. The authors would like to thank Mr. M. Benak for his comments on the English manuscript.

APPENDIX I: RIEMANN SOLVER AND FVS METHOD

Riemann solver[16]

The first method for the discretization of the inviscid fluxes is a finite volume Riemann solver.[16] The method is constructed by splitting the Euler equations into two one-dimensional equations

$$(JQ)_t + E_\xi = 0, \tag{6}$$

$$(JQ)_t + G_\zeta = 0. \tag{7}$$

The Riemann solver defines the conservative variables on the cell faces as a function of the corresponding conservative variables at the characteristics (denoted by the index $j = 0, 1, 2$). The conservative variables used for the discretization of the inviscid flux E in equation (6) (similarly the flux G in equation (7)) are defined as[16]

$$\rho = \rho_0 + R_1 + R_2, \tag{8}$$

$$l = l_0 + (u + s\tilde{x})R_1 + (u - s\tilde{x})R_2, \tag{9}$$

$$n = n_0 + (w + s\tilde{z})R_1 + (w - s\tilde{z})R_2, \tag{10}$$

$$e = e_0 + (H + s\lambda_0)R_1 + (H - s\lambda_0)R_2. \tag{11}$$

The terms R_1 and R_2 are defined as

$$R_1 = \frac{1}{2s^2}\left[(\rho_0 - \rho_1)\left(s\lambda_0 - \frac{\gamma - 1}{2}q^2\right) + (l_0 - l_1)[(\gamma - 1)u - s\tilde{x}] + (n_0 - n_1)[(\gamma - 1)w - s\tilde{z}] - (l_0 - l_1)(\gamma - 1)\right]. \tag{12a}$$

$$R_2 = \frac{1}{2s^2}\left[-(\rho_0 - \rho_2)\left(s\lambda_0 + \frac{\gamma - 1}{2}q^2\right) + (l_0 - l_2)[(\gamma - 1)u + s\tilde{x}] + (n_0 - n_2)[(\gamma - 1)w + s\tilde{z}] - (l_0 - l_2)(\gamma - 1)\right], \tag{12b}$$

where

$$\tilde{x} = \frac{\xi_x}{\sqrt{(\xi_x^2 + \xi_z^2)}}, \qquad \tilde{z} = \frac{\xi_z}{\sqrt{(\xi_x^2 + \xi_z^2)}}, \tag{13}$$

$$q^2 = u^2 + w^2, \tag{14}$$

while λ_0, λ_1, and λ_2 are the eigenvalues defined as

$$\lambda_0 = u\tilde{x} + w\tilde{z}, \qquad \lambda_1 = \lambda_0 + s, \qquad \lambda_2 = \lambda_0 - s, \tag{15}$$

where s is the speed of sound. The terms ρ_j, $l_j = (\rho u)_j$, $n_j = (\rho w)_j$ and e_j with $j = 0, 1, 2$ are the characteristic conservative variables. Similarly, the conservative variables can be defined for the inviscid flux G.

The characteristic conservative variables on the cell faces are calculated from the left or right side of the cell face in accordance with the sign of the eigenvalues (Godunov-type differencing):

$$Q^j_{i+1/2} = \tfrac{1}{2}\{[1 + \text{sign}(\lambda_j)]Q^-_{i+1/2} + [1 - \text{sign}(\lambda_j)]Q^+_{i+1/2}\} \quad \text{for } j = 0, 1, 2. \tag{16}$$

Modified Steger–Warming flux-vector-splitting (FVS) method

The modified FVS method splits the flux $E_{i+1/2}$ (similarly the fluxes $G_{k+1/2}$ and $G_{k-1/2}$) on the cell face $i + 1/2$ instead of on the centre of the volume for higher accuracy in the boundary layers:

$$E_{i+1/2} = E^+_{i+1/2} + E^-_{i-1/2}. \tag{17}$$

The original Steger–Warming FVS method[7] causes large numerical diffusion as well as entropy errors in some flow regions. Improvement of the method is obtained by modification of the eigenvalue splitting. Because at vanishing zeroth eigenvalue the mass flux is not differentiable and FVS cannot be applied, the zeroth eigenvalue is split as a function of the first and second eigenvalues:

$$\lambda_0^{\pm} = \frac{\lambda_1^{\pm} + \lambda_2^{\pm}}{2}. \tag{18}$$

The second modification concerns the definition of the energy term of the split fluxes. A negative influence of FVS method on the conservation of total enthalpy emerges by the formulation of

the energy flux. Improvement is obtained by discretization of the energy flux in terms of the total enthalpy H. Finally the convective flux is defined as

$$E^{\pm}_{i+1/2}(Q^{\mp}) = J\rho\sqrt{(\xi_x^2 + \xi_z^2)}\begin{pmatrix} \frac{1}{2}(\lambda_1^{\pm} + \lambda_2^{\pm}) \\ (u + s\tilde{x}/\gamma)\lambda_1^{\pm}/2 + (u - s\tilde{x}/\gamma)\lambda_2^{\pm}/2 \\ (w + s\tilde{z}/\gamma)\lambda_1^{\pm} + (w - s\tilde{z}/\gamma)\lambda_2^{\pm}/2 \\ \frac{1}{2}H^{\pm}(\lambda_1^{\pm} + \lambda_2^{\pm}) \end{pmatrix}, \tag{19}$$

where

$$\lambda_j^{\pm} = \frac{\lambda_j \pm |\lambda_j|}{2} \quad \text{for } j = 1, 2. \tag{20}$$

APPENDIX II: HIGH-ORDER EXTRAPOLATION SCHEMES

Five-point extrapolation scheme

The left and right states of conservative variables on the cell faces are defined by a hybrid upwind scheme. This is a five-point scheme constructed by superposition of the first-, second-, third- and fourth-order extrapolation formulae as[16]

$$Q^{\pm}_{i+1/2} = AQ^{1;\pm}_{i+1/2} + (1 - A)\{BQ^{2;\pm}_{i+1/2} + (1 - B)[CQ^{3;\pm}_{i+1/2} + (1 - C)Q^{4;\pm}_{i+1/2}]\}. \tag{21}$$

The superscripts 1–4 denote the orders of the extrapolation. For instance, the third- and fourth-order extrapolations are defined respectively as

$$(Q^3_{i+1/2})^- = \tfrac{1}{6}(5Q_i - Q_{i-1} + 2Q_{i+1}), \qquad (Q^3_{i+1/2})^+ = \tfrac{1}{6}(5Q_{i+1} - Q_{i+2} + 2Q_i),$$

$$(Q^4_{i+1/2})^- = (Q^4_{i+1/2})^+ = \tfrac{1}{12}(7Q_i + 7Q_{i+1} - Q_{i-1} - Q_{i+2}).$$

The terms A and B are limiter functions defined by the squares of the second-order derivatives of pressure:

$$A = \min(1, a|p^2_{\xi\xi,i+1} - p^2_{\xi\xi,i}|), \qquad B = \min(1, b|p^2_{\xi\xi,i+1} + p^2_{\xi\xi,i}|).$$

The values of the constants a and b in the last relations are $a = 4{\cdot}5$ and $b = 2{\cdot}5$, while the constant C in (21) is $C = 2.25$ for the fourth-order scheme and $C = 1$ for third-order accuracy. If the parameter b has large values, the scheme switches to second-order accuracy.

MUSCL scheme

The second class of upwind extrapolation schemes which are implemented in the present work is the monotone upstream centred scheme for conservation law (MUSCL).[17] The conservative variables using the MUSCL scheme are defined as

$$Q^-_{i+1/2} = Q_i + \frac{S_i}{4}[(1 - kS_i)\nabla + (1 + kS_i)\Delta]Q_i, \tag{22a}$$

$$Q^+_{i+1/2} = Q_{i+1} - \frac{S_{i+1}}{4}[(1 + kS_{i+1})\nabla + (1 - kS_{i+1})\Delta]Q_{i+1}, \tag{22b}$$

with $\Delta Q_i = Q_{i+1} - Q_i$ and $\nabla Q_i = Q_i - Q_{i-1}$. S is the van Albada limiter function for the detection of shocks and other discontinuities:

$$S_i = \frac{2\nabla Q_i \Delta Q_i}{(\nabla Q_i)^2 + (\Delta Q_i)^2 + \varepsilon},$$

where ε is a small number ($\varepsilon = 10^{-5}$) in order to prevent division by zero. The spatial accuracy depends on the parameter k: $k = -1$ produces a fully upwinded, $k = 0$ a symmetric, $k = \frac{1}{3}$ a third-order-biased and $k = 1$ a centred scheme.

Central differences are used for the discretization of the second-order derivatives of the viscous terms. For the cross-derivatives an 'upwind'-type scheme[25] is used.

REFERENCES

1. D. A. Johnson, C. C. Horstman and W. D. Bachalo, 'Comparison between experiment and prediction for a transonic turbulent separated flow', *AIAA J.*, **20**, 737–744 (1982).
2. J. M. Delery, 'Shock wave/turbulent boundary layer interaction and its control', *Prog. Aerospace Sci.*, **22**, 209–280 (1985).
3. J. Sahu and J. Danberg, 'Navier–Stokes computations of transonic flows with a two equation turbulence model', *AIAA J.*, **24**, 1744–1751 (1986).
4. U. C. Goldberg and S. R. Chakravarthy, 'Predictions of separated flows with a new backflow turbulence model', *AIAA J.*, **26**, 405–408 (1988).
5. U. C. Goldberg, B. L. Bihari and S. V. Ramakrishnan, 'Model for turbulent backflows', *AIAA J.*, **30**, 557–559 (1992).
6. T. J. Coackley and M. V. Bergmann, 'Effects of turbulence model selection on the prediction of complex aerodynamic flows', *AIAA Paper 79-0070*, 1979.
7. J. L. Steger and R. F. Warming, 'Flux vector splitting of the inviscid gasdynamic equations with applications to finite-difference methods.' *J. Comput. Phys.*, **40**, 263–293 (1981).
8. B. van Leer, 'Flux-vector splitting for the Euler equations.' *Lecture Notes in Physics*, Vol. 170, Springer, Berlin, 1982, pp. 507–512.
9. W. K. Anderson, J. L. Thomas and B. van Leer, 'Comparison of finite volume flux vector splittings for the Euler equations', *AIAA J.*, **24**, 1453–1460 (1986).
10. P. L. Roe, 'Approximate Riemann solvers, Parameters vectors and difference schemes', *J. Comput. Phys.*, **43**, 337–365 (1981).
11. H. C. Yee and A. Harten, 'Implicit TVD schemes for hyperbolic conservation laws in curvilinear coordinates.' *AIAA J.*, **25**, (1987).
12. B. van Leer, J. L. Thomas, P. L. Roe and R. W. Newsome, 'A comparison of flux formulas for the Euler and Navier–Stokes equations', *AIAA Paper 87-1184*, AIAA 8th CFD Conference 1987.
13. W. J. Coirier and B. van Leer, 'Numerical flux formulas for the Euler and Navier–Stokes equations II. Progress in flux-vector splitting, *NASA TM 104353*, 1991.
14. M. S. Liou and C. Steffen Jr., 'A new flux splitting scheme', *NASA TM 104404*, 1991.
15. D. Drikakis and S. Tsangaris, 'On the solution of Navier–Stokes equations using improved flux vector splitting methods', *Appl. Math. Modell.*, **17**, 282–297 (1993).
16. A. Eberle, 'Characteristic flux averaging approach to the solution of Euler's equations', *VKI Lecture Series, Computational Fluid Dynamics, 1987-04*, 1987.
17. B. van Leer, 'Towards the ultimate conservative difference scheme. V: A second order sequel to Godunov's method', *J. Comput. Phys.*, **32**, 101–136 (1979).
18. R. W. MacCormack and C. V. Candler 'The solution of the Navier–Stokes equations using Gauss–Seidel line relaxation', *Comput. Fluids*, **17**, 135–150 (1989).
19. B. Koren, 'Upwind discretization of the steady Navier–Stokes equations', *Int. j. numer. methods fluids*, **11**, 99–117 (1990).
20. D. Drikakis and S. Tsangaris, 'On the accuracy and efficiency of CFD methods in real gas hypersonics', *Int. j. numer. methods fluids*, **16**, 759–775 (1993).
21. M. A. Schmatz, A. Brenneis and A. Eberle, 'Verification of an implicit relaxation method for steady and unsteady viscous flow problems, *AGARD CP 437*, 1988, pp. 15-1–15-33.
22. B. S. Baldwin and H. Lomax, 'Thin layer approximation and algebraic model for separated turbulent flows', *AIAA Paper 78-257*, AIAA 16th Aerosp. Sc. Meeting, 1978.
23. J. W. Kooi, 'Influence of free stream Mach number on transonic shock-wave/boundary layer interactions', *NLR MP-78013 U*, 1978.
24. T. L. Holst, 'Viscous transonic airfoil workshop. Compendium of results', *AIAA Paper 87-1460*, AIAA 19th Fluid Dynamics, Plasma Dynamics and Laser Conference, 1987.
25. S. R. Chakravarthy, 'High resolution upwind formulations for the Navier–Stokes equations', *VKI Lecture Series, Computational Fluid Dynamics, 1988-05*, 1988.